Title

Clamping enables enhanced electromechanical responses in antiferroelectric thin films

Journal

Nature Materials, 23(7)

ISSN

1476-1122

Authors

Pan, Hao

Zhu, Menglin

Banyas, Ella

et al.

Publication Date

2024-07-01

DOI

10.1038/s41563-024-01907-y

nature materials

Article

https://doi.org/10.1038/s41563-024-01907-y

Clamping enables enhanced electromechanical responses in antiferroelectric thin films

Received: 1 November 2023

Accepted: 24 April 2024

Published online: 23 May 2024

Check for updates

Hao Pan[1,11], Menglin Zhu[2,11], Ella Banyas[3,4,11], Louis Alaerts[5], Megha Acharya[1,3], Hongrui Zhang[1,3], Jiyeob Kim[1], Xianzhe Chen[1,3], Xiaoxi Huang[1], Michael Xu[2], Isaac Harris[4], Zishen Tian[1,3], Francesco Ricci[3,4], Brendan Hanrahan[6], Jonathan E. Spanier[7], Geoffroy Hautier[5], James M. LeBeau[2], Jeffrey B. Neaton[3,4,8] & Lane W. Martin[1,3,9,10]

Thin-film materials with large electromechanical responses are fundamental enablers of next-generation micro-/nano-electromechanical applications. Conventional electromechanical materials (for example, ferroelectrics and relaxors), however, exhibit severely degraded responses when scaled down to submicrometre-thick films due to substrate constraints (clamping). This limitation is overcome, and substantial electromechanical responses in antiferroelectric thin films are achieved through an unconventional coupling of the field-induced antiferroelectric-to-ferroelectric phase transition and the substrate constraints. A detilting of the oxygen octahedra and lattice-volume expansion in all dimensions are observed commensurate with the phase transition using *operando* electron microscopy, such that the in-plane clamping further enhances the out-of-plane expansion, as rationalized using first-principles calculations. In turn, a non-traditional thickness scaling is realized wherein an electromechanical strain (1.7%) is produced from a model antiferroelectric $PbZrO_3$ film that is just 100 nm thick. The high performance and understanding of the mechanism provide a promising pathway to develop high-performance micro-/nano-electromechanical systems.

Electromechanical transduction has been a fundamental enabler of various modern technologies including actuators, resonators, ultrasonic imaging and so on, in which electromechanical strain produced by an applied electric field is a key parameter[1,2]. Current field standards are ferroelectric and relaxor-ferroelectric ceramics and crystals, among which the best can produce strain values of ~1.0% due to their high piezoelectricity[2–4]. When such materials are scaled down to submicrometre-thick films, however, the achievable strains and piezoelectric responses are considerably reduced (in some cases by over an order of magnitude)[5,6] because the mechanical constraints from the substrate (so-called clamping) can restrict the polarization rotation and lattice deformation, which are the keys to the large effects[7]. To overcome the substrate constraints, various strategies have been explored such as lateral scaling[8], constructing nanopillar-like structures[9] and leveraging oxygen-vacancy redistribution[10]. While interesting, such approaches can be complicated and are not always compatible with the desired application scenarios. Such substrate constraints are critical obstacles in developing micro-/nano-electromechanical systems with

A full list of affiliations appears at the end of the paper. e-mail: lwmartin@rice.edu

https://doi.org/10.1038/s41563-024-01907-y

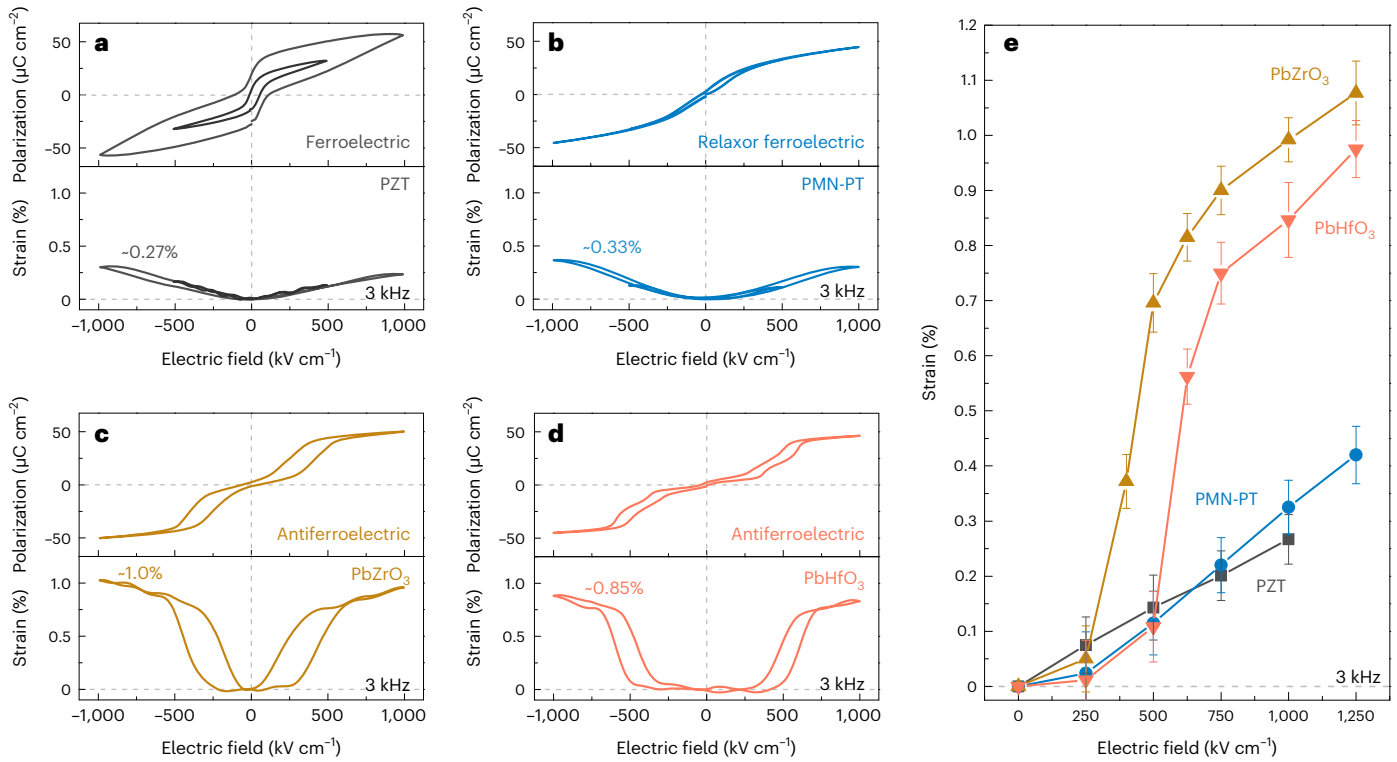

Fig. 1 | Electromechanical response of typical (relaxor) ferroelectric and antiferroelectric thin films. a–**d**, Polarization/electric-field hysteresis loops (top) and electromechanical-strain/electric-field loops (bottom) for $PbZr_{0.52}Ti_{0.48}O_3$ (PZT) ferroelectric films (**a**) and $0.67PbMg_{1/3}Nb_{2/3}O_3$–$0.33PbTiO_3$ (PMN-PT) relaxor ferroelectric films (**b**) as well as $PbZrO_3$ (**c**) and $PbHfO_3$ (**d**) antiferroelectric films. All films are 100 nm thick and are measured at a frequency of 3 kHz. **e**, Comparison of the electromechanical strain values of the ferroelectric and antiferroelectric thin films at various electric fields; data are mean and s.d. from 25 repeated measurements.

higher performance and lower power consumption and in enabling further miniaturization[11].

Antiferroelectrics, on the other hand, which exhibit antipolar order at zero field and a reversible field-induced transition to polar order (ferroelectric phase)[12,13], can also exhibit large electromechanical responses (0.4–0.8%) and have been considered as potential candidates for such devices[14,15]. Antiferroelectrics should have no piezoelectric response because of the antipolar (macroscopically non-polar) ground-state symmetry; instead, their electromechanical response arises from the lattice-volume change associated with the field-driven antiferroelectric-to-ferroelectric phase transition[16,17]. Intriguingly, sub-micrometre-thick antiferroelectrics have been reported to demonstrate comparable electromechanical responses to those obtained in bulk versions[18–20], in stark contrast to what is observed in (relaxor) ferroelectrics. The mechanism for this 'absence' of thickness scaling in the electromechanical response of antiferroelectrics remains to be clarified. Such an understanding, particularly of the underlying roles of the phase transition and the substrate clamping, would be important for both fundamental materials science and practical application of antiferroelectrics as electromechanical materials.

Here, combining epitaxial thin-film growth, electrical and electromechanical measurements, *operando* field-dependent scanning transmission electron microscopy (STEM) and first-principles calculations, the electric-field-induced antiferroelectric-to-ferroelectric phase transition has been studied and an unconventional coupling of the phase transition with the substrate constraints is revealed to manifest as a large electromechanical response. Focusing on the model antiferroelectric $PbZrO_3$, a detilting of the oxygen octahedra is found to occur commensurate with the field-induced phase transition from the antiferroelectric (orthorhombic, *Pbam*) to the ferroelectric (rhombohedral, *R*3*m*) phase, which results in an abrupt lattice-volume expansion. Such an expansion should happen in all directions, but the substrate constraints restrict the in-plane expansion and focus the volume expansion in the out-of-plane direction, thus enhancing the electromechanical response (instead of degrading it as in (relaxor) ferroelectrics) and resulting in a non-traditional thickness scaling. A high electromechanical strain (~1.7%) is thus achieved in $PbZrO_3$ films just 100 nm thick by controlling the orientation and thickness to take the best advantage of the phase transition and substrate constraints. These responses are robust with frequency (from 0.2 to 100 kHz), and exhibit only slight fatigue out to 10^8 cycles. The high performance and understanding of these antiferroelectric thin films provides opportunities to overcome the general scaling obstacles for electromechanical materials and to develop high-performance micro-/nano-electromechanical systems.

Electromechanical response in antiferroelectric films

To compare the electromechanical responses of antiferroelectric and ferroelectric films, 100-nm-thick epitaxial films of the antiferroelectrics $PbZrO_3$ and $PbHfO_3$, and the canonical ferroelectric $PbZr_{0.52}Ti_{0.48}O_3$ and relaxor ferroelectric $0.67PbMg_{1/3}Nb_{2/3}O_3$–$0.33PbTiO_3$ were synthesized via pulsed-laser deposition and fabricated into symmetric capacitor structures (Methods). All films are single crystalline and epitaxial, as characterized using X-ray diffraction and reciprocal space mapping (Supplementary Fig. 1). The electric-field-dependent polarization and out-of-plane electromechanical responses of the films were measured using established approaches integrating a ferroelectric tester and a laser Doppler vibrometer[21] (Methods). In the ferroelectric $PbZr_{0.52}Ti_{0.48}O_3$ (Fig. 1a) and the relaxor ferroelectric $0.67PbMg_{1/3}Nb_{2/3}O_3$–$0.33PbTiO_3$ (Fig. 1b) films, clear polarization hysteresis loops are observed along with electromechanical strains that increase monotonically with field, reaching ~0.27% and ~0.33%,

https://doi.org/10.1038/s41563-024-01907-y

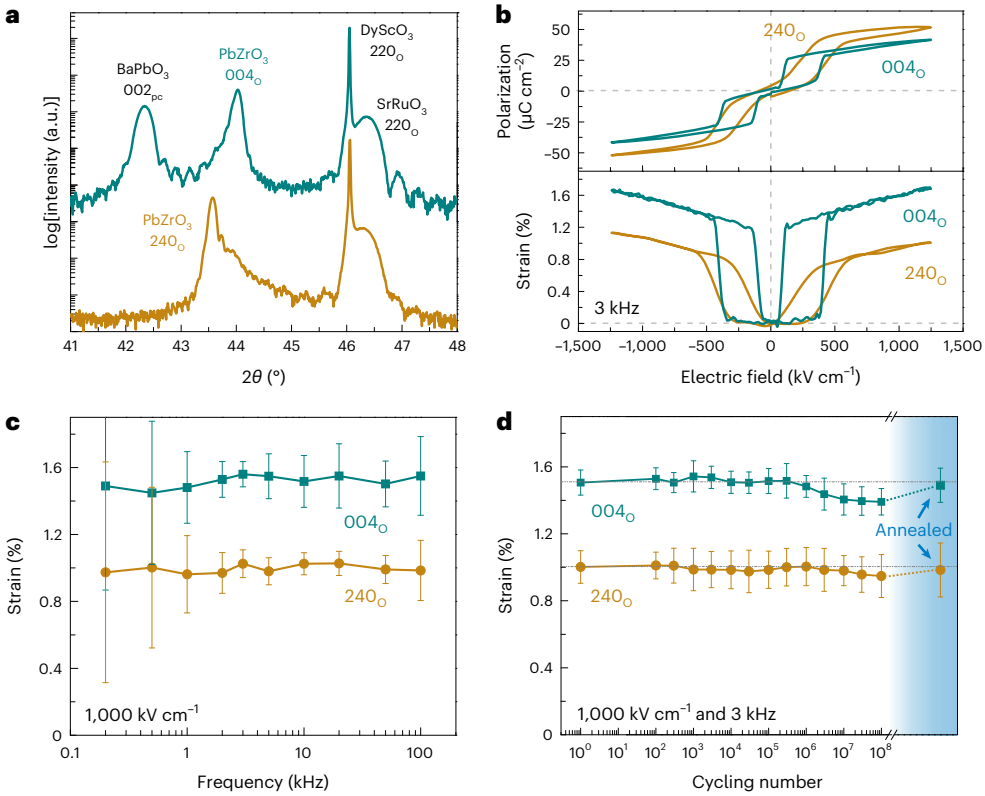

Fig. 2 | Enhanced electromechanical response in orientation-engineered $PbZrO_3$ antiferroelectric thin films. a, X-ray diffraction (2theta–omega) scans of 40 nm $SrRuO_3$/100 nm $PbZrO_3$/30 nm $SrRuO_3$/$DyScO_3$ $(110)_O$ (gold curve) and 40 nm $SrRuO_3$/100 nm $PbZrO_3$/40 nm $BaPbO_3$/30 nm $SrRuO_3$/$DyScO_3$ $(110)_O$ (green curve) heterostructures where the $PbZrO_3$ films exhibit $(240)_O$ (that is, $(100)_{pc}$ or $(010)_{pc}$, gold curve) and $(004)_O$ (that is, $(001)_{pc}$) orientations, respectively. 2θ, the angle between the transmitted beam and reflected beam. **b**, Polarization (top) and electromechanical response (bottom) as a function of electric field in the orientation-engineered $PbZrO_3$ thin films at 3 kHz. **c**, Frequency dependence of the electromechanical response of the orientation-engineered $PbZrO_3$ thin films at an electric field of 1,000 kV cm^{-1}. **d**, Electromechanical response of the orientation-engineered $PbZrO_3$ thin films at 1,000 kV cm^{-1} and 3 kHz over 10^8 cycles and after annealing at 400 °C for one hour in oxygen. Data are mean and s.d. from 25 repeated measurements.

respectively, at 1,000 kV cm^{-1}. These strains are substantially smaller as compared to bulk-version materials (for example, 0.57% strain at 50 kV cm^{-1} in $PbZr_{0.52}Ti_{0.48}O_3$ ceramics[22] and 0.75% strain at 130 kV cm^{-1} in $0.67PbMg_{1/3}Nb_{2/3}O_3$–$0.33PbTiO_3$ crystals[3]) and thicker films (for example, ~0.75% strain at 1,000 kV cm^{-1} and ~1.0% at 1,400 kV cm^{-1} in 350-nm-thick $0.7PbMg_{1/3}Nb_{2/3}O_3$–$0.3PbTiO_3$ films[8]). Such considerable degradation in thin films highlights the dominant impact that substrate clamping of lattice deformation can have on the piezoelectric response wherein it limits both polarization rotation and domain-wall motion under a field[6,7]. Meanwhile, in the antiferroelectric $PbZrO_3$ (Fig. 1c) and $PbHfO_3$ (Fig. 1d) films, characteristic double polarization hysteresis loops are observed with a distinctly different electromechanical behaviour: an abrupt 'jump' of the response at fields between 300 and 600 kV cm^{-1}, commensurate with the field-induced antiferroelectric-to-ferroelectric phase transition. This gives rise to large strains of ~1.0% and ~0.85% for $PbZrO_3$ and $PbHfO_3$, respectively, at 1,000 kV cm^{-1}; these values are >2.5 times those obtained in the (relaxor) ferroelectric films of the same thickness (Fig. 1e) and reach/surpass the responses of much thicker relaxor films (~0.75% at 1,000 kV cm^{-1} for 350-nm-thick $0.7PbMg_{1/3}Nb_{2/3}O_3$–$0.3PbTiO_3$ films[8]). Such electromechanical responses are among the highest values previously reported for antiferroelectric crystals, ceramics and micrometre-thick layers and indicate a distinctly different substrate clamping effect from that observed in (relaxor) ferroelectrics.

For brevity, we focus further analysis of the antiferroelectric films on the archetypal $PbZrO_3$. At zero field, $PbZrO_3$ exhibits an orthorhombic (*Pbam*) unit cell with $\sqrt{2} \times 2\sqrt{2} \times 2$ pseudocubic perovskite lattice parameters such that $a_{pc} \approx b_{pc} \approx a_O/\sqrt{2} \approx b_O/(2\sqrt{2}) \approx 4.15$ Å, and $c_{pc} \approx c_O/2 \approx 4.10$ Å ('O' and 'pc' denote orthorhombic and pseudocubic, respectively; Supplementary Fig. 2)[12]. The $PbZrO_3$ films are grown on $SrRuO_3$-buffered $DyScO_3(110)_O$ substrates and are $(240)_O$ oriented ($(100)_{pc}$ or $(010)_{pc}$ oriented; Supplementary Fig. 2), with the shorter c_{pc} lying in plane for a smaller lattice mismatch with $DyScO_3$ ($a_{pc} \approx 3.95$ Å). This means that the 1.0% electromechanical response in the $PbZrO_3$ films (Fig. 1c) is the result of the lattice expansion along the a_{pc} or b_{pc} axis during the antiferroelectric-to-ferroelectric transition. For a comprehensive understanding of the lattice evolution, it is imperative to also study the electromechanical response along the c_{pc} axis, which is structurally anisotropic from the a_{pc} and b_{pc} axes. To do this, $(004)_O$-oriented (that is, $(001)_{pc}$-oriented) $PbZrO_3$ films were synthesized (Fig. 2a). Here, a 40-nm-thick $BaPbO_3$ conductive buffer layer (with pseudocubic lattice constants of ~4.27 Å)[23] was inserted between $PbZrO_3$ and the bottom $SrRuO_3$ electrode to induce the a_{pc} and b_{pc} axes of $PbZrO_3$ to lie in plane (Supplementary Figs. 2 and 3). The resulting 100-nm-thick, $(004)_O$-oriented $PbZrO_3$ films exhibit a similar field-induced antiferroelectric-to-ferroelectric phase transition but even sharper increases in both polarization and electromechanical response, with the latter reaching a value of ~1.7% at 1,250 kV cm^{-1} (Fig. 2b). This value is 55% larger than that in the $(240)_O$-oriented $PbZrO_3$ films, and four to five times the values in the $PbZr_{0.52}Ti_{0.48}O_3$ and $0.67PbMg_{1/3}Nb_{2/3}O_3$–$0.33PbTiO_3$ films (Fig. 1).

The robustness of the electromechanical responses was also probed for the $(004)_O$-oriented and $(240)_O$-oriented $PbZrO_3$ films as a function of frequency (Fig. 2c). Films with both orientations exhibit reversible antiferroelectric-to-ferroelectric transitions with stable, large electromechanical responses over the range of 0.2–100 kHz

(Fig. 2c and Supplementary Fig. 4). Note that the increased standard deviation at frequencies <1 kHz is from lower-frequency ambient noise that impacts the electromechanical measurements[21]. At higher frequencies (for example, 100 kHz), a frequency limit exists in the experimental configuration, which results in a higher probability of signal distortion[21] (Supplementary Fig. 4) and increased standard deviation. The actual upper frequency limit of the reversible antiferroelectric-to-ferroelectric transition is found to be >1 MHz (Supplementary Note 1 and Supplementary Figs. 5 and 6). Similarly, the evolution of the electromechanical responses with repeated cycling reveals that both the $(004)_O$- and $(240)_O$-oriented $PbZrO_3$ films maintain high electromechanical strain values with only a modest reduction (<8%) over 10^8 cycles (Fig. 2d). This slight fatigue is ascribed to the gradual accumulation of defects that pin the antiferroelectric-to-ferroelectric phase boundaries[24]. Such effects can be remedied with light annealing (one hour at 400 °C in 760 mtorr of oxygen), after which the pinned phase boundaries are freed from the defects and the original responses are recovered (Supplementary Fig. 7). Such performance recovery with annealing is robust over repeated rounds of cycling (up to 10^8 cycles) and annealing (Supplementary Fig. 8), and is effective even after 10^9 cycles (Supplementary Fig. 9), which provides a simple way to improve the lifespan of the materials.

Operando STEM characterization of the phase transition

To better understand the high electromechanical responses of the antiferroelectric thin films, it is critical to reveal the lattice-structure evolution during the antiferroelectric-to-ferroelectric phase transition, and how the substrate clamping interacts with the antiferroelectric films in a manner different from that in (relaxor) ferroelectric films. To shed light on these mysteries, field-dependent, *operando* STEM studies were conducted on the evolution of the lattice during the phase transition using a sample holder that could apply voltages across the sample (Methods and Supplementary Fig. 10). A representative cross-sectional dark-field image of a $(004)_O$-oriented $PbZrO_3$ heterostructure at zero field (Fig. 3a) reveals areas with varied contrast corresponding to antiferroelectric domains with perpendicular polarization orientations along the $[110]_{pc}$ and $[1\bar{1}0]_{pc}$. A nano-beam electron diffraction (NBED) pattern taken along the $[221]_{pc}$ zone axis reveals well-resolved $¼\{110\}_{pc}$ superlattice reflections (Fig. 3b), a key characteristic of antiferroelectricity (antiparallel lead-cation displacements in a ↑↑↓↓ pattern that causes the quadrupling of the unit cell along the $<110>_{pc}$)[25]. An NBED pattern taken along the $[110]_{pc}$ zone axis reveals another set of $½\{111\}_{pc}$ superlattice reflections (Fig. 3c), which are ascribed to the antiphase tilting (opposite rotations in successive layers) of the oxygen octahedra around the $<100>_{pc}$ in the antiferroelectric lattice[26].

Upon increasing the voltage (field) across the $PbZrO_3$ material in the STEM instrument in 1 V (100 kV cm^{-1}) steps, the antiferroelectric phase remains stable until 5 V (500 kV cm^{-1}), above which the domains transform into a uniform contrast (Fig. 3d) and the $¼\{110\}_{pc}$ reflections disappear (Fig. 3e), indicating the onset of the antiferroelectric-to-ferroelectric phase transition. The NBED patterns (Fig. 3c,f) allow for the extraction of the $PbZrO_3$ lattice constants (Methods), which are $a_{pc} \approx 4.150$ Å (in plane) and $c_{pc} \approx 4.115$ Å (out of plane) in the antiferroelectric phase at zero field, and $a_{pc} \approx c_{pc} \approx 4.150$ Å in the ferroelectric phase at high fields. While this agrees with the general proposition that the field-induced ferroelectric phase is rhombohedral, there are ongoing discussions on whether the ferroelectric phase exhibits *R*3*c* (with antiphase oxygen-octahedral tilting) or *R*3*m* (without octahedral tilting) symmetry[26,27]. The observation here that the $½\{111\}_{pc}$ reflections almost vanish at high fields (Fig. 3f) suggests that the oxygen-octahedra tilting is reduced to nearly zero (that is, octahedral detilting) in the ferroelectric phase, which is more consistent with the *R*3*m* symmetry. In addition, weak $½\{110\}_{pc}$ reflections

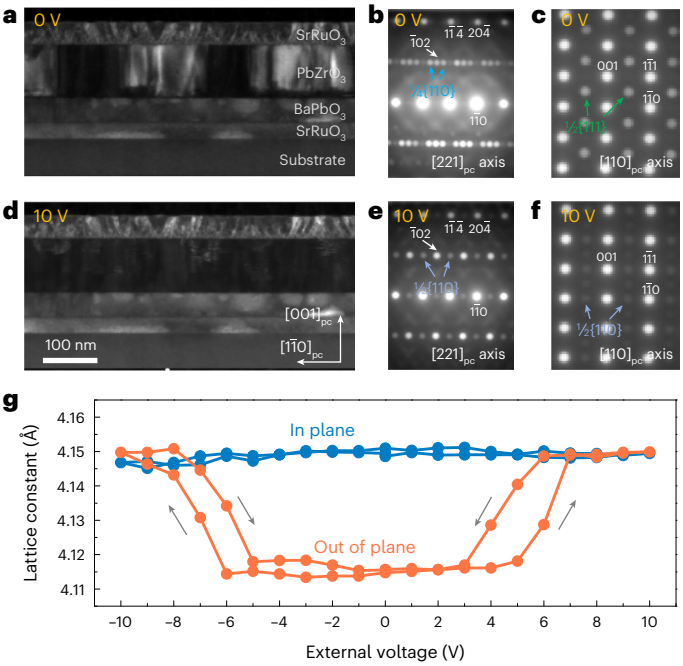

Fig. 3 | *Operando* STEM studies of the phase transition and structural evolution in $(004)_O$-oriented $PbZrO_3$ thin films. a–c, Structure of the pristine antiferroelectric phase of the $PbZrO_3$ thin films including a STEM cross-sectional dark-field image (**a**) and NBED patterns along the $[221]_{pc}$ (**b**) and $[110]_{pc}$ (**c**) zone axes. **d–f**, Structure of the field-induced ferroelectric phase of the $PbZrO_3$ thin films (with an external voltage of 10 V) including a STEM cross-sectional dark-field image (**d**) and NBED patterns along the $[221]_{pc}$ (**e**) and $[110]_{pc}$ (**f**) zone axes. **g**, Evolution of the in-plane ($(100)_{pc}$) or ($(010)_{pc}$)) and out-of-plane ($(001)_{pc}$) lattices of the $PbZrO_3$ films with respect to external voltage cycles between −10 and 10 V.

are noted in the field-induced ferroelectric phase (Fig. 3e,f); such reflections were also observed in ferroelectric zirconium-rich $PbZr_{1-x}Ti_xO_3$, which has *R*3*m* symmetry (the high-temperature rhombohedral ferroelectric in the $PbZr_{1-x}Ti_xO_3$ phase diagram)[28], and are ascribed to residual antiparallel cation displacements[29] (Supplementary Note 2).

In perovskite crystals, oxygen-octahedral tilting is a key mechanism to accommodate structural distortion[30]; such octahedral detilting during the voltage-induced antiferroelectric-to-ferroelectric (*Pbam*-to-*R*3*m*) transition should thus cause a substantial lattice deformation and electromechanical response. This transition is reversible, as revealed by the disappearance/reappearance of the superlattice reflections and reversible domain transformation (Supplementary Video 1). The voltage-dependent evolution of the lattice constants of the $PbZrO_3$ (Fig. 3g) further reveals that while the out-of-plane lattice c_{pc} exhibits distinct expansion (shrinkage) commensurate with the antiferroelectric-to-ferroelectric (and vice versa) transition, the in-plane lattice a_{pc} (which is clamped by the substrate) effectively does not change. Similar reversible antiferroelectric-to-ferroelectric transitions are also observed *operando* in the $(240)_O$-oriented $PbZrO_3$ films, in which the c_{pc} axis lies in plane and becomes clamped (Supplementary Fig. 11 and Supplementary Note 3). Taken together, these observations provide microscopic supporting evidence showing consistent behaviours to those in macroscopic observations (Fig. 2), and moreover suggest that the substrate constraints indeed interact with the lattice and should make a substantial impact on the phase transitions and electromechanical properties in the antiferroelectric thin films.

Enhanced response via substrate constraint

Based on the understanding of the phase transition and substrate constraints from the *operando* STEM studies, first-principles density

https://doi.org/10.1038/s41563-024-01907-y

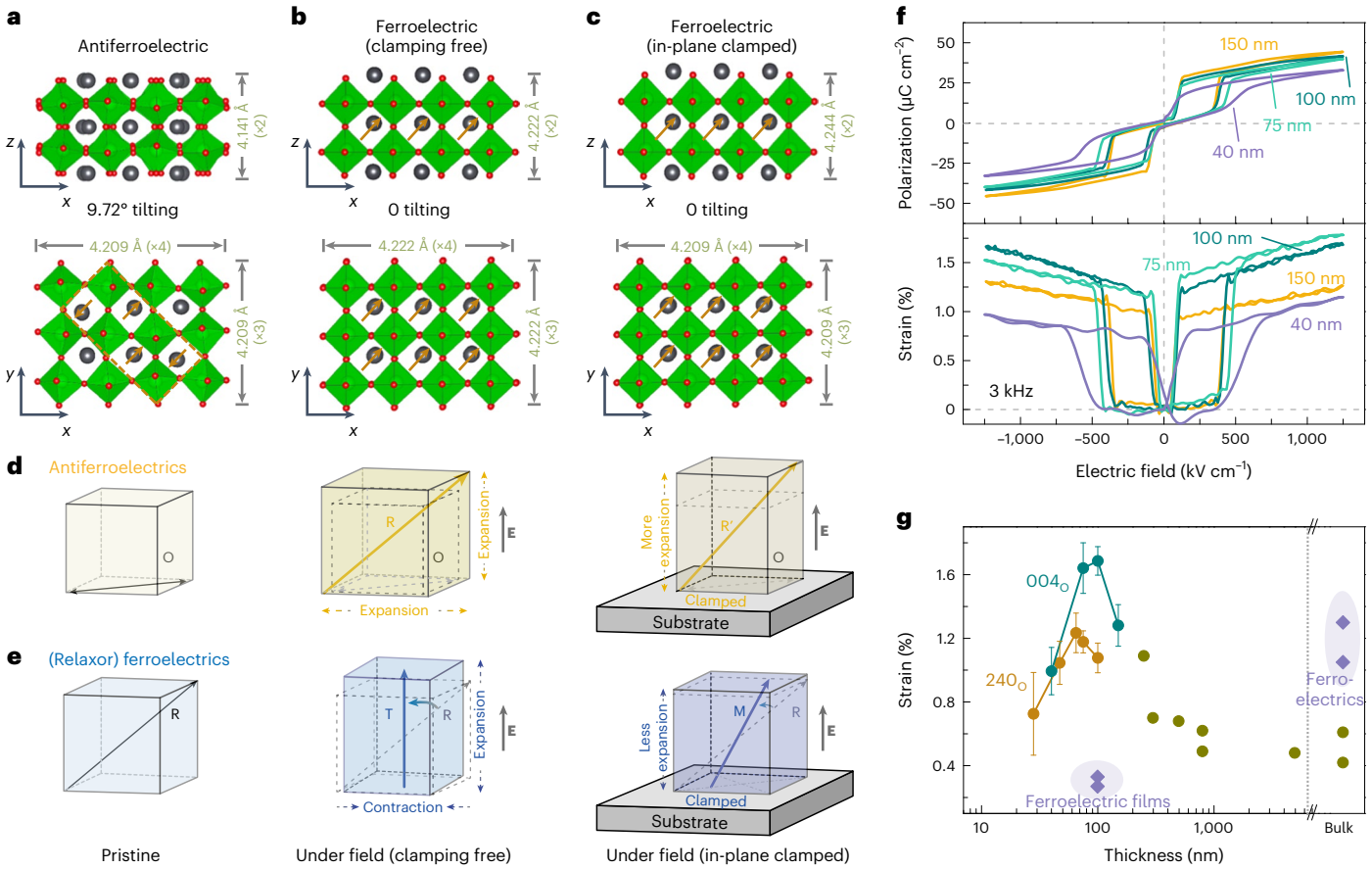

Fig. 4 | Mechanism for the enhancement of electromechanical response and abnormal thickness scaling in antiferroelectric $PbZrO_3$ thin films. **a**–**c**, First-principles calculation of the atomic structures of $PbZrO_3$ in the ground-state antiferroelectric phase (**a**), metastable ferroelectric phase (clamping-free condition; **b**) and ferroelectric phase with a preset in-plane clamping condition (mimicking the substrate constraints on a $(004)_O$-oriented $PbZrO_3$ film; **c**). The orange arrows denote the (projected) polarization directions of the lead cations. **d**, Schematic illustrations of a pristine antiferroelectric lattice (orthorhombic (O), left) and the lattice deformations (electromechanical responses) due to field-induced antiferroelectric-to-ferroelectric phase transitions in a clamping-free condition (rhombohedral (R), middle) and in-plane clamped condition (distorted rhombohedral (R'), right); the field is denoted by **E**. The arrows inside the lattices denote the polarization directions. **e**, Comparative schematic illustrations of a pristine (relaxor) ferroelectric lattice (rhombohedral (R), left) and the lattice deformations (electromechanical responses) due to field-induced polarization rotation in a clamping-free condition (tetragonal (T), middle) and in-plane clamped condition (monoclinic (M), right). **f**, Polarization (top) and electromechanical responses (bottom) as a function of applied field in $(004)_O$-oriented $PbZrO_3$ films of various thicknesses. **g**, Comparison of the electromechanical strain values of $PbZrO_3$ films in this work (blue-green and gold circles) and other $PbZrO_3$-based antiferroelectric films and ceramics in the literature (pickle-green circles)[14,15,18–20,37–39]. Data are mean and s.d. from 25 repeated measurements. Electromechanical strain values of the (relaxor) ferroelectric films in this work and typical ferroelectric ceramics and crystals in the literature (purple diamonds)[2,4] are also shown for comparison.

functional theory (DFT) calculations were used to further shed light on the mechanism of the large electromechanical responses in the $PbZrO_3$ thin films (Methods). An unconstrained relaxation of the ground-state orthorhombic (*Pbam*) antiferroelectric structure of $PbZrO_3$ was performed with the Perdew–Burke–Ernzerhof exchange–correlation functional[31,32], and the lattice parameters were computed to be $a_{pc} \approx b_{pc} \approx 4.209$ Å and $c_{pc} \approx 4.141$ Å (Fig. 4a), close to the experimental values[12]. The structure is characterized by antiparallel lead-cation displacements along the $<110>_{pc}$ (macroscopically non-polar) and antiphase titling of the oxygen octahedra about the $[100]_{pc}$ and $[010]_{pc}$ axes (with tilting angles of ~9.72°), consistent with the $¼\{110\}_{pc}$ and $½\{111\}_{pc}$ superlattice reflections in STEM. A similar relaxation of the metastable *R*3*m* polar phase of $PbZrO_3$ was also performed in an unconstrained (that is, clamping-free) state (Fig. 4b), the formation energy of which was found to be 1.82 meV per formula unit higher than that of the antiferroelectric *Pbam* ground state (Supplementary Note 4). The *R*3*m* structure possesses parallel lead-cation displacements along the $<111>_{pc}$ with a calculated polarization of 42.6 μC cm^{-2} projected along the $<100>_{pc}$ axes (Methods). The oxygen-octahedra tilting angles are found to decrease to almost zero along all $<100>_{pc}$ axes in the *R*3*m* phase, consistent with the disappearance of the $½\{111\}_{pc}$ reflections in STEM (Fig. 3f). As a direct result of the octahedral detilting, the *R*3*m* structure exhibits increased lattice parameters of 4.222 Å (with lattice angles of ~89.3°) and an auxetic volume expansion as compared to the *Pbam* structure[16,33]; that is, the lattice expands in all directions (by 0.28% along a_{pc} and b_{pc}, and by 1.93% along c_{pc}; Fig. 4b). These results qualitatively rationalize the observed electromechanical responses but do not reproduce the experimental data quantitatively. First, for the $(240)_O$-oriented $PbZrO_3$, the calculated lattice expansion (0.28% along the out-of-plane a_{pc}) arising from the *Pbam*-to-*R*3*m* transition is much smaller than the experimentally observed electromechanical strain of ~1.0%, indicating additional factors contributing to the response. Second, the calculated in-plane lattice parameters of the unconstrained $PbZrO_3$ also expand with the phase transition, which is something not observed experimentally in either $(240)_O$- or $(004)_O$-oriented $PbZrO_3$ films due to substrate clamping (Fig. 3g and Supplementary Fig. 11).

To address these discrepancies, calculations were performed for substrate-clamped versions of the polar structures of $PbZrO_3$.

To account for clamping, the in-plane lattice of the polar structures was subjected to strain minimization (with symmetry preservation) with respect to the pristine *Pbam* phase, and the out-of-plane lattice was allowed to relax through an iterative process (Supplementary Note 4 and Supplementary Fig. 12). For example, in clamped, polar $(004)_O$-oriented $PbZrO_3$ (Fig. 4c), the in-plane lattice parameters a_{pc} and b_{pc} were fixed as 4.209 Å (the same as *Pbam*), values that are smaller than the clamping-free *R*3*m* lattice parameters (4.222 Å; Fig. 4b) and equivalent to an in-plane biaxial compression of ~0.3%. The calculated polar structure with such in-plane clamping (compression) exhibits a further expanded out-of-plane lattice parameter c_{pc} from 4.222 Å to 4.244 Å, corresponding to an enhanced electromechanical response from 1.93% to 2.46% (with respect to the pristine *Pbam* lattice). Despite the auxeticity in the *Pbam*-to-*R*3*m* transition, the *R*3*m* phase itself has been shown to be Poissonian[27], with a Poisson's ratio of ~0.34, by elastic-tensor calculations. This, at the atomic level, is correlated with a slightly distorted *R*3*m* structure with elongated octahedra along c_{pc} (while octahedral tilting angles remain minimal; Fig. 4c). Likewise, in the clamped, polar $(240)_O$-oriented $PbZrO_3$, the substrate constraints are computed to give rise to an even larger in-plane compression of 1.1%, which leads to a more substantial enhancement of the out-of-plane lattice expansion from 0.28% to 1.91% (Supplementary Fig. 13 and Supplementary Table 1). Additional details related to the energetics of this field-induced phase transition are also provided (Supplementary Note 5 and Supplementary Fig. 14). These calculations demonstrate an unconventional coupling between the antiferroelectric-to-ferroelectric transition and the substrate constraints, wherein the in-plane lattice expansion from the octahedral detilting during the phase transition is clamped by the substrate, which in turn focuses the volume expansion in the out-of-plane direction, thereby producing an enhanced electromechanical response (schematic in Fig. 4d). This effect is robust, with stable performance and intact film structures (no cracking or other noticeable changes) over repeated antiferroelectric-to-ferroelectric transition cycles (Fig. 2d and Supplementary Fig. 15).

This understanding helps explain why (relaxor) ferroelectrics have reduced electromechanical responses in clamped thin films while antiferroelectric films behave differently. The high electromechanical responses in (relaxor) ferroelectrics come from polarization rotations (for example, from $[111]_{pc}$ to $[001]_{pc}$ under a field along the $[001]_{pc}$)[34,35], with lattice expansion along the field but contraction perpendicular to the field (Fig. 4e). This contrasts with antiferroelectrics, where lattice expansion occurs in all directions. In (relaxor) ferroelectric films on substrates, the clamping mechanically inhibits the in-plane contraction, hinders the polarization rotation from accessing the full range of symmetries (for example, from rhombohedral R, to monoclinic M (including M_A and M_C or monoclinic symmetries with slightly different polarization directions), to tetragonal T, as observed in $PbMg_{1/3}Nb_{2/3}O_3$–$PbTiO_3$)[7,36] and thus reduces the out-of-plane electromechanical response (Fig. 4e). The mechanical constraints imposed by substrate clamping are more substantial in thinner films as the mechanical clamping is interface-based[21], such that the electromechanical response decreases as the ferroelectric films get thinner[5,6]. By contrast, an increased electromechanical response with reduced thickness should be expected in antiferroelectric films, considering the positive impact from substrate constraints. To explore this concept, a thickness series of both $(004)_O$- and $(240)_O$-oriented $PbZrO_3$ films was produced (28–150 nm thick; Supplementary Fig. 16), and the electromechanical responses (Fig. 4f and Supplementary Fig. 17) were compared, together with those of previously reported $PbZrO_3$-based antiferroelectric films and ceramics (Fig. 4g)[14,15,18–20,37–39]. Upon reducing the film thickness, the electromechanical responses of the antiferroelectric films indeed exhibit (initially) an increasing trend and reach a peak of ~1.7% at 75–100 nm in the $(004)_O$-oriented films and ~1.2% at 65–75 nm in the $(240)_O$-oriented films, indicating an abnormal thickness scaling behaviour opposite to that of conventional electromechanical (ferroelectric, relaxor) materials[5–7]. Yet as the thickness is further reduced, the electromechanical response of the $PbZrO_3$ films starts to decrease (along with a reduction of the field-induced polarization; Fig. 4f and Supplementary Fig. 17). This behaviour is ascribed to the $PbZrO_3$–electrode interfaces, where defects could potentially pin the antiferroelectric-to-ferroelectric phase transition, reducing the polarizability and electromechanical responses (Supplementary Fig. 18). This interface-related performance degradation is negligible in thick materials but becomes dominant in ultrathin films (similar to that in dielectric/ferroelectric thin films)[40]. Nevertheless, a high electromechanical response of >0.72% is still maintained even in 28-nm-thick $PbZrO_3$ films.

Outlook

This work highlights the potential of antiferroelectric thin films as electromechanical material candidates that can overcome the general performance degradation with reduced thickness in traditional (relaxor) ferroelectrics. It also provides insights into the atomic structural evolution during the antiferroelectric-to-ferroelectric transition and its coupling with substrate clamping at the unit cell scale, which synergistically enhance the electromechanical response in antiferroelectric films. The resulting non-traditional thickness dependence of the electromechanical responses and the large values of strain (~1.7%) realized in 100-nm-thick, orientation-engineered $PbZrO_3$ films (with robust frequency stability and fatigue resistance) provide a promising pathway to address the general scaling obstacles and to develop high-performance electromechanical materials at the nanometre scale. It is anticipated that further efforts to control the composition[41], orientation[42] and microstructure[43] could increase the breakdown strength and lower the phase-transition fields of the antiferroelectric films, further promoting their application in integrated micro-/nano-electromechanical systems with better reliability and lower energy consumption.

Online content

Any methods, additional references, Nature Portfolio reporting summaries, source data, extended data, supplementary information, acknowledgements, peer review information; details of author contributions and competing interests; and statements of data and code availability are available at https://doi.org/10.1038/s41563-024-01907-y.

References

1. Cross, L. E. Ferroelectric materials for electromechanical transducer applications. *Mater. Chem. Phys.* **43**, 108–115 (1996).
2. Narayan, B. et al. Electrostrain in excess of 1% in polycrystalline piezoelectrics. *Nat. Mater.* **17**, 427–431 (2018).
3. Park, S. & Shrout, T. R. Ultrahigh strain and piezoelectric behavior in relaxor based ferroelectric single crystals. *J. Appl. Phys.* **82**, 1804–1811 (1997).
4. Huangfu, G. et al. Giant electric field-induced strain in lead-free piezoceramics. *Science* **378**, 1125–1130 (2022).
5. Kim, D. M. et al. Thickness dependence of structural and piezoelectric properties of epitaxial $Pb(Zr_{0.52}Ti_{0.48})O_3$ films on Si and $SrTiO_3$ substrates. *Appl. Phys. Lett.* **88**, 142904 (2006).
6. Xu, F. et al. Domain wall motion and its contribution to the dielectric and piezoelectric properties of lead zirconate titanate films. *J. Appl. Phys.* **89**, 1336–1348 (2001).
7. Kim, J. et al. Coupled polarization and nanodomain evolution underpins large electromechanical responses in relaxors. *Nat. Phys.* **18**, 1502–1509 (2022).
8. Keech, R. et al. Lateral scaling of $Pb(Mg_{1/3}Nb_{2/3})O_3$-$PbTiO_3$ thin films for piezoelectric logic applications. *J. Appl. Phys.* **115**, 234106 (2014).
9. Liu, H. et al. Giant piezoelectricity in oxide thin films with nanopillar structure. *Science* **369**, 292–297 (2020).
10. Park, D. S. et al. Induced giant piezoelectricity in centrosymmetric oxides. *Science* **375**, 653–657 (2022).

11. Eom, C. & Trolier-McKinstry, S. Thin-film piezoelectric MEMS. *MRS Bull.* **37**, 1007–1017 (2012).
12. Randall, C. A., Fan, Z., Reaney, I., Chen, L. Q. & Trolier-McKinstry, S. Antiferroelectrics: history, fundamentals, crystal chemistry, crystal structures, size effects, and applications. *J. Am. Ceram. Soc.* **104**, 3775–3810 (2021).
13. Mischenko, A. S., Zhang, Q., Scott, J. F., Whatmore, R. W. & Mathur, N. D. Giant electrocaloric effect in thin-film $PbZr_{0.95}Ti_{0.05}O_3$. *Science* **311**, 1270–1271 (2006).
14. Berlincourt, D. Transducers using forced transitions between ferroelectric and antiferroelectric states. *IEEE Trans. Sonics Ultrason.* **13**, 116–124 (1966).
15. Zhuo, F. et al. Large field-induced strain, giant strain memory effect, and high thermal stability energy storage in (Pb,La)(Zr,Sn,Ti)O_3 antiferroelectric single crystal. *Acta Mater.* **148**, 28–37 (2018).
16. Liu, H. et al. Electric-field-induced structure and domain texture evolution in $PbZrO_3$-based antiferroelectric by *in-situ* high-energy synchrotron X-ray diffraction. *Acta Mater.* **184**, 41–49 (2020).
17. Lu, H. et al. Probing antiferroelectric-ferroelectric phase transitions in $PbZrO_3$ capacitors by piezoresponse force microscopy. *Adv. Funct. Mater.* **30**, 2003622 (2020).
18. Xu, B., Ye, Y. & Cross, L. E. Dielectric properties and field-induced phase switching of lead zirconate titanate stannate antiferroelectric thick films on silicon substrates. *J. Appl. Phys.* **87**, 2507–2515 (2000).
19. Nadaud, K. et al. Dielectric, piezoelectric and electrostrictive properties of antiferroelectric lead-zirconate thin films. *J. Alloy. Compd.* **914**, 165340 (2022).
20. Yao, Y. et al. Ferrielectricity in the archetypal antiferroelectric, $PbZrO_3$. *Adv. Mater.* **35**, 2206541 (2023).
21. Acharya, M. et al. Direct measurement of inverse piezoelectric effects in thin films using laser Doppler vibrometry. *Phys. Rev. Appl.* **20**, 14017 (2023).
22. Li, J. et al. Lead zirconate titanate ceramics with aligned crystallite grains. *Science* **380**, 87–93 (2023).
23. Boldyreva, K. et al. Microstructure and electrical properties of $(120)_O$-oriented and of $(001)_O$-oriented epitaxial antiferroelectric $PbZrO_3$ thin films on (100) $SrTiO_3$ substrates covered with different oxide bottom electrodes. *J. Appl. Phys.* **102**, 44111 (2007).
24. Pan, H. et al. Defect-induced, ferroelectric-like switching and adjustable dielectric tunability in antiferroelectrics. *Adv. Mater.* **35**, 2300257 (2023).
25. Ma, T. et al. Uncompensated polarization in incommensurate modulations of perovskite antiferroelectrics. *Phys. Rev. Lett.* **123**, 217602 (2019).
26. Lu, T. et al. Critical role of the coupling between the octahedral rotation and *A*-site ionic displacements in $PbZrO_3$-based antiferroelectric materials investigated by *in situ* neutron diffraction. *Phys. Rev. B* **96**, 214108 (2017).
27. Tan, X., Ma, C., Frederick, J., Beckman, S. & Webber, K. G. The antiferroelectric ↔ ferroelectric phase transition in lead-containing and lead-free perovskite ceramics. *J. Am. Ceram. Soc.* **94**, 4091–4107 (2011).
28. Ricote, J. et al. A TEM and neutron diffraction study of the local structure in the rhombohedral phase of lead zirconate titanate. *J. Phys. Condens. Matter* **10**, 1767–1786 (1998).
29. Woodward, D. I., Knudsen, J. & Reaney, I. M. Review of crystal and domain structures in the $PbZr_xTi_{1-x}O_3$ solid solution. *Phys. Rev. B* **72**, 104110 (2005).
30. Glazer, A. M. The classification of tilted octahedra in perovskites. *Acta Cryst.* **B28**, 3384–3392 (1972).
31. Reyes-Lillo, S. E. & Rabe, K. M. Antiferroelectricity and ferroelectricity in epitaxially strained $PbZrO_3$ from first principles. *Phys. Rev. B* **88**, 180102 (2013).
32. Lisenkov, S., Yao, Y., Bassiri-Gharb, N. & Ponomareva, I. Prediction of high-strain polar phases in antiferroelectric $PbZrO_3$ from a multiscale approach. *Phys. Rev. B* **102**, 104101 (2020).
33. Park, S., Pan, M., Markowski, K., Yoshikawa, S. & Cross, L. E. Electric field induced phase transition of antiferroelectric lead lanthanum zirconate titanate stannate ceramics. *J. Appl. Phys.* **82**, 1798–1803 (1997).
34. Fu, H. X. & Cohen, R. E. Polarization rotation mechanism for ultrahigh electromechanical response in single-crystal piezoelectrics. *Nature* **403**, 281–283 (2000).
35. Noheda, B. et al. Polarization rotation via a monoclinic phase in the piezoelectric 92% $PbZn_{1/3}Nb_{2/3}O_3$-8% $PbTiO_3$. *Phys. Rev. Lett.* **86**, 3891–3894 (2001).
36. Brewer, A. et al. Microscopic piezoelectric behavior of clamped and membrane (001) PMN-30PT thin films. *Appl. Phys. Lett.* **119**, 202903 (2021).
37. Tani, T., Li, J. F., Viehland, D. & Payne, D. A. Antiferroelectric-ferroelectric switching and induced strains for sol-gel derived lead zirconate thin layers. *J. Appl. Phys.* **75**, 3017–3023 (1994).
38. Maiwa, H. & Ichinose, N. Electrical and electromechanical properties of $PbZrO_3$ thin films prepared by chemical solution deposition. *Jpn. J. Appl. Phys.* **40**, 5507–5510 (2001).
39. Sharifzadeh Mirshekarloo, M., Yao, K. & Sritharan, T. Large strain and high energy storage density in orthorhombic perovskite $(Pb_{0.97}La_{0.02})(Zr_{1-x-y}Sn_xTi_y)O_3$ antiferroelectric thin films. *Appl. Phys. Lett.* **97**, 142902 (2010).
40. Tagantsev, A. K. & Gerra, G. Interface-induced phenomena in polarization response of ferroelectric thin films. *J. Appl. Phys.* **100**, 51607 (2006).
41. Acharya, M. et al. Exploring the $Pb_{1-x}Sr_xHfO_3$ system and potential for high capacitive energy storage density and efficiency. *Adv. Mater.* **34**, 2105967 (2022).
42. Liu, C. et al. Low voltage-driven high-performance thermal switching in antiferroelectric $PbZrO_3$ thin films. *Science* **382**, 1265–1269 (2023).
43. Zhang, J. X. et al. Large field-induced strains in a lead-free piezoelectric material. *Nat. Nanotechnol.* **6**, 98–102 (2011).

[1]Department of Materials Science and Engineering, University of California, Berkeley, CA, USA. [2]Department of Materials Science and Engineering, Massachusetts Institute of Technology, Cambridge, MA, USA. [3]Materials Sciences Division, Lawrence Berkeley National Laboratory, Berkeley, CA, USA. [4]Department of Physics, University of California, Berkeley, CA, USA. [5]Thayer School of Engineering, Dartmouth College, Hanover, NH, USA. [6]DEVCOM Army Research Laboratory, Adelphi, MD, USA. [7]Department of Mechanical Engineering and Mechanics, Materials Science and Engineering, and Physics, Drexel University, Philadelphia, PA, USA. [8]Kavli Energy Nanosciences Institute, University of California, Berkeley, Berkeley, CA, USA. [9]Departments of Materials Science and NanoEngineering, Chemistry, and Physics and Astronomy, Rice University, Houston, TX, USA. [10]Rice Advanced Materials Institute, Rice University, Houston, TX, USA. [11]These authors contributed equally: Hao Pan, Menglin Zhu, Ella Banyas. ✉e-mail: lwmartin@rice.edu

Methods

Epitaxial thin-film growth

$PbZrO_3$ thin films with $(240)_O$ orientation were grown as 40 nm $SrRuO_3$/100 nm $PbZrO_3$/30 nm $SrRuO_3$/$DyScO_3$ $(110)_O$ (Crystec) heterostructures; and $PbZrO_3$ thin films with $(004)_O$ orientation were grown as 40 nm $SrRuO_3$/100 nm $PbZrO_3$/40 nm $BaPbO_3$/30 nm $SrRuO_3$/$DyScO_3$ $(110)_O$ heterostructures via pulsed-laser deposition using a KrF excimer laser (240 nm, LPX 300, Coherent). In both cases, the growth was completed in an on-axis growth geometry with a target-to-substrate spacing of 5.5 mm and from ceramic targets of the noted compositions. The targets were sanded, cleaned and sufficiently pre-ablated prior to each growth. The bottom electrode $SrRuO_3$ (~30 nm) was deposited at a heater temperature of 700 °C in a dynamic oxygen pressure of 100 mTorr, at a laser fluence of ~1.4 J cm^{-2} and a laser repetition rate of 15 Hz. The $BaPbO_3$ layer, which serves as both an electrode and a buffer layer for the $(004)_O$-oriented growth of $PbZrO_3$, was deposited at a heater temperature of 550 °C in a dynamic oxygen pressure of 100 mTorr, at a laser fluence of ~0.7 J cm^{-2} and a laser repetition rate of 2 Hz. The $PbZrO_3$ layer was subsequently grown at a heater temperature of 600 °C in a dynamic oxygen pressure of 80 mTorr, at a laser fluence of ~1.3 J cm^{-2} and a laser repetition rate of 5 Hz. Finally, the top electrode $SrRuO_3$ was deposited in situ after the $PbZrO_3$ growth with the same growth parameters as the bottom $SrRuO_3$ layer, but at a reduced heater temperature of 550 °C to reduce the potential volatilization of lead from the $PbZrO_3$. The heterostructures were then cooled to room temperature at a rate of 10 °C min^{-1} in a static oxygen pressure of 700 Torr. For comparison, thin $PbHfO_3$, PZT and PMN-PT layers of ~100 nm were also synthesized in the form of $SrRuO_3$/$PbHfO_3$/$SrRuO_3$/$SrTiO_3$ (001), $SrRuO_3$/PZT/$SrRuO_3$/$SrTiO_3$ (001) and $(Ba_{0.5}Sr_{0.5})RuO_3$/PMN-PT/$(Ba_{0.5}Sr_{0.5})RuO_3$/$NdScO_3$ $(110)_O$ heterostructures, respectively, with separately optimized pulsed-laser deposition processes. The detailed deposition parameters for these materials can be found in previous reports[7,21,41].

Structural characterization

X-ray line scans and reciprocal space mapping studies of the heterostructures were conducted with a high-resolution X-ray diffractometer (copper source, $K_{\alpha 1}$ radiation of wavelength 1.5406 Å; Panalytical, X'pert^3 MRD), using a hybrid two-bounce primary monochromator to generate the incident X-ray beam and a PIXcel3D position-sensitive detector. The line scans were performed in a symmetric set-up with a 1/2° receiving slit and a point detector. The scanning speed is 0.01° and 0.5 s per step. The reciprocal space mappings were obtained in an asymmetric set-up around the 332_O-diffraction condition of $DyScO_3$, with a 1/16° receiving slit and a line detector (with an active length of 2.51° in the 2θ angle). The scanning speed is 0.01° (in omega angle) and 4 s per step.

Electrical and electromechanical measurements

Capacitor structures are fabricated via photolithography and etching for all electrical-related measurements. To do this, an OCG 825 (G-line positive) photoresist layer was spin-coated on the heterostructures, exposed under a photoresist mask and then developed and patterned into arrays of circles with diameters of 50 μm. The top $SrRuO_3$ or $Ba_{0.5}Sr_{0.5}RuO_3$ layer was then selectively etched by either a $NaIO_4$ aqueous solution (0.1 mol l^{-1}) or ion milling to realize circular capacitor structures. Polarization-electric-field hysteresis loops were measured with a bipolar triangular voltage profile using a Precision Ferroelectric Tester (Radiant Technologies). The electromechanical responses of the heterostructure thin films (glued on a rigid glass slide) were characterized by a non-contact single-beam laser Doppler vibrometer (VibroOne VIO-130, PolyTech) integrated with the Precision Ferroelectric Tester. A 1.5-μm-diameter laser spot (HeNe laser with a wavelength of 633 nm) was focused vertically on the thin films (on the capacitor structures with diameters of 50 μm), whose electromechanical response (that is, surface displacement) under an applied field was measured via the (Doppler) frequency shift of the back-scattered laser beam, which has a high sensitivity of ~2 pm (ref. 21). The electromechanical strain value was defined as the ratio of the surface displacement to the thickness of the ferroelectric or antiferroelectric film, which was calculated as the average of values in 25 repeated measurements. Experimental evidence and detailed discussions are provided (Supplementary Fig. 19 and Supplementary Note 6) that demonstrate that substrate bending is negligible and does not contribute to the electromechanical measurements in these devices.

Scanning transmission electron microscopy

STEM sample preparation and *operando* electrical (voltage) biasing studies were conducted on both $(240)_O$- and $(004)_O$-oriented $PbZrO_3$ thin-film heterostructures. To ensure robust electrical connection and voltage application, the $PbZrO_3$ heterostructures were grown with the same parameters on conductive Nb:$SrTiO_3$ $(001)_{pc}$ substrates (working as bottom electrodes), which did not affect the film orientations or microstructures as $PbZrO_3$ was always relaxed from the substrates. A platinum top layer was also grown as a robust top electrode. A cross-sectional lamella (20 μm in length) was then extracted from the heterostructure using the focused ion beam technique with the FEI Helios Nanolab 600 focused ion beam and scanning electron microscopy system, following the standard lift-out procedure. Subsequently, the lamella was transferred between the two electrodes of a dedicated micro-electromechanical system chip (Supplementary Fig. 10). The sample was then thinned to electron transparency (~50 nm thick) using a focused ion beam, with the gallium-beam energy gradually decreasing from 30 to 5 kV. Finally, two trenches were created on each side with a focused ion beam. The left-side trench removed all materials below the top electrode (platinum), and the right one removed all materials above the bottom electrode (substrate; Supplementary Fig. 10). This geometry ensured an out-of-plane voltage biasing across the film during the *operando* experiments, mimicking the set-up in the macroscopic measurements.

Four-dimensional STEM (4D-STEM) investigations on the samples were carried out using a probe-aberration-corrected Thermo Fisher Scientific Themis Z G2 microscope equipped with an Electron Microscopy Pixel Array Detector[44]. NBED patterns were captured in a grid across the whole film area. The datasets were obtained while the microscope was operated at 200 kV, with an estimated beam current of 80 pA and a semi-convergence angle of approximately 0.8 mrad. *Operando* biasing of the $PbZrO_3$ film was accomplished using a DENSsolutions Lightning transmission electron miscroscopy holder. Voltage application and measurement were simultaneously conducted using a four-point probe configuration with a Keithley 2450 source measuring unit, which was controlled by the DENSsolutions Impulse software. Throughout the experiment, the sample underwent voltage bias cycling with a step size of 1 V between consecutive voltage points. To ensure uniformity and mitigate potential spatial disparities, the 4D-STEM datasets were acquired from approximately the same region for each voltage level. All datasets were subsequently aligned by registering the virtual dark-field image generated from the corresponding 4D-STEM dataset. This alignment procedure ensured that the extraction of structural and lattice information was consistently performed on an identical region.

The lattice parameters of the $PbZrO_3$ films under different voltages were extracted by the exit-wave power-cepstrum (EWPC) analysis of the corresponding NBED patterns[45]. The underlying principle of EWPC involves conducting a discrete Fourier transform on the logarithm of a convergent beam electron diffraction pattern, thereby yielding real-space lattice spacing information with subpicometre precision[45,46]. Additionally, the impact of sample tilt on the calculated lattice parameters can be mitigated. An illustrative NBED pattern alongside its corresponding EWPC pattern is presented (Supplementary Fig. 20). Thus, by

measuring peak distances in the EWPC patterns, the average projected in-plane and out-of-plane lattice parameters were quantified.

First-principles calculations

DFT calculations were performed with the Vienna Ab initio Simulation Package[47,48] using projector augmented-wave pseudopotentials[49,50]. Electrons explicitly treated as valence were $4s^2 4p^6 5s^1 4d^3$ for zirconium, $5d^{10} 6s^2 6p^2$ for lead and $2s^2 2p^4$ for oxygen. Calculations were performed using the generalized gradient approximation of Perdew–Burke–Ernzerhof[51] unless otherwise noted. A plane-wave energy cut-off of 600 eV was used for the Vienna Ab initio Simulation Package calculations. The *Pbam* structure was optimized on a gamma-centred grid of 12 × 4 × 8 k points, and the *R*3*m* structures were optimized on a grid of 12 × 12 × 12 k points. Gaussian smearing with a width of 0.01 eV was used to perform geometry optimizations, and static total-energy calculations were performed with the tetrahedron method. The force convergence threshold was set to 10^{-3} eV Å^{-1}, and the electronic self-consistency convergence threshold was 10^{-7} eV.

Manipulation of the fully optimized structures was performed with the pymatgen Python package[52]. The processing workflow is shown (Supplementary Fig. 12). First, the *Pbam* structure was oriented along the epitaxial $(240)_O$ and $(004)_O$, and the rhombohedral structures were transformed to matching settings. 'Clamping' of the rhombohedral in-plane lattice parameters *a* and *b* was accomplished by minimizing their total strain with respect to the corresponding *Pbam* lattice parameters, subject to the constraint that the rhombohedral symmetry be reduced to monoclinic (*Cm*) at the lowest. The *c* axes of the rhombohedral phases were optimized through iterative distortion (Supplementary Fig. 12), until the out-of-plane expansion of the cells (measured with respect to the *Pbam* structure) converged to within 0.005% for the $(004)_O$ orientation and 0.05% for the $(240)_O$ orientation.

The ferroelectric polarization of the rhombohedral phases were calculated with the Berry phase method[53,54] as implemented within the atomate Python package[55], with the *Pbam* structure taken as the non-polar reference. Elastic tensors were calculated from a finite-differences approach using a plane-wave energy cut-off of 750 eV and a 16 × 16 × 16 k-point grid. Nudged elastic band calculations were performed using the same parameters as initially described with the exceptions of the k-point sampling, which was done with a 6 × 2 × 4 grid, and the force convergence threshold, which was set to 0.02 eV Å^{-1}. The unit cells were kept frozen during all nudged elastic band calculations. For both the free-standing (unclamped) and clamped cases, we used 16 images constructed by linear interpolation between the *Pbam* and *R*3*m* phases, and computed the spontaneous polarization of each image post-relaxation with the Berry phase method.

Data availability

All data supporting the findings of this study are available within the article and its Supplementary Information. Additional data are available from the corresponding author upon request.

Code availability

Detailed information related to the codes of the DFT calculations used in this study is available from the corresponding author upon request.

References

44. Tate, M. W. et al. High dynamic range pixel array detector for scanning transmission electron microscopy. *Microsc. Microanal.* **22**, 237–249 (2016).
45. Padgett, E. et al. The exit-wave power-cepstrum transform for scanning nanobeam electron diffraction: robust strain mapping at subnanometer resolution and subpicometer precision. *Ultramicroscopy* **214**, 112994 (2020).
46. Shao, Y. et al. Cepstral scanning transmission electron microscopy imaging of severe lattice distortions. *Ultramicroscopy* **231**, 113252 (2021).
47. Kresse, G. & Furthmuller, J. Efficient iterative schemes for *ab initio* total-energy calculations using a plane-wave basis set. *Phys. Rev. B* **54**, 11169–11186 (1996).
48. Kresse, G. & Furthmüller, J. Efficiency of ab-initio total energy calculations for metals and semiconductors using a plane-wave basis set. *Comput. Mater. Sci.* **6**, 15–50 (1996).
49. Blöchl, P. E. Projector augmented-wave method. *Phys. Rev. B* **50**, 17953–17979 (1994).
50. Kresse, G. & Joubert, D. From ultrasoft pseudopotentials to the projector augmented-wave method. *Phys. Rev. B* **59**, 1758–1775 (1999).
51. Perdew, J. P., Burke, K. & Ernzerhof, M. Generalized gradient approximation made simple. *Phys. Rev. Lett.* **77**, 3865–3868 (1996).
52. Ong, S. P. et al. Python Materials Genomics (pymatgen): a robust, open-source Python library for materials analysis. *Comput. Mater. Sci.* **68**, 314–319 (2013).
53. King-Smith, R. D. & Vanderbilt, D. Theory of polarization of crystalline solids. *Phys. Rev. B* **47**, 1651–1654 (1993).
54. Resta, R. Macroscopic polarization in crystalline dielectrics: the geometric phase approach. *Rev. Mod. Phys.* **66**, 899–915 (1994).
55. Mathew, K. et al. Atomate: a high-level interface to generate, execute, and analyze computational materials science workflows. *Comput. Mater. Sci.* **139**, 140–152 (2017).

Acknowledgements

We thank T.J. Lee and O. Ashour for fruitful discussions. This work was funded by the US Department of Energy, Office of Science, Office of Basic Energy Sciences, Materials Sciences and Engineering Division under contract no. DE-AC02-05CH11231 (Materials Project programme KC23MP) for the development of functional materials. H.P., B.H., J.E.S., J.M.L. and L.W.M. acknowledge the support of the Army Research Laboratory under Cooperative Agreements W911NF-19-2-0119 and W911NF-24-2-0100. J.K. acknowledges the support of the US Army Research Office under grant W911NF-21-1-0118. Z.T. acknowledges the support of the US Department of Energy, Office of Science, Office of Basic Energy Sciences, under award no. DE-SC-0012375 for the development of complex oxide thin-film heterostructures. X.H. and I.H. acknowledge the support of the SRC-JUMP ASCENT centre. H.Z. acknowledges the support of the US Department of Defense, Air Force Office of Scientific Research under grant no. FA9550-18-1-0480. E.B. acknowledges support from the US National Science Foundation Graduate Research Fellowship under grant no. 1752814. Computational resources were provided by the National Energy Research Scientific Computing Center (NERSC), a US Department of Energy, Office of Science User Facility located at Lawrence Berkeley National Laboratory, operated under contract no. DE-AC02-05CH11231. J.E.S. and L.W.M. acknowledge additional support from the Army Research Office under grant W911NF-21-1-0126.

Author contributions

H.P. and L.W.M. conceived and designed this study. H.P., M.A., J.K. and I.H. deposited films. H.P., H.Z. and X.C. prepared the capacitor samples. H.P., X.H. and Z.T. performed the electrical and electromechanical measurements. M.Z., M.X. and J.M.L. conducted the STEM studies. E.B., L.A., F.R., G.H. and J.B.N. conducted the first-principles calculations. B.H. and J.E.S. provided feedback and insights on antiferroelectric materials and helped with analysis of the findings. The manuscript was written by H.P. and L.W.M., with contributions from all others. All authors discussed the results and revised the manuscript.

Competing interests

The authors declare no competing interests.

Additional information

Supplementary information The online version contains supplementary material available at https://doi.org/10.1038/s41563-024-01907-y.

Correspondence and requests for materials should be addressed to Lane W. Martin.

Peer review information *Nature Materials* thanks Ying-Hao Chu, Ming-Min Yang and the other, anonymous, reviewer(s) for their contribution to the peer review of this work.